THE EUROPEAN
PHYSICAL JOURNAL A

A concept for the extraction of the most refractory elements at CERN-ISOLDE as carbonyl complex ions

J. Ballof[1,2,8,a] , **K. Chrysalidis**[1,5], **Ch. E. Düllmann**[2,3,4], **V. Fedosseev**[1], **E. Granados**[1], **D. Leimbach**[1,5],
B. A. Marsh[1], **J. P. Ramos**[1,6,9], **A. Ringvall-Moberg**[1,7], **S. Rothe**[1], **T. Stora**[1,b], **S. G. Wilkins**[1], **A. Yakushev**[3,4,6]

[1] Accelerator Systems Department, CERN, Geneva, Switzerland
[2] Department of Chemistry - TRIGA Site, Johannes Gutenberg University, Mainz, Germany
[3] GSI Helmholtzzentrum für Schwerionenforschung, Darmstadt, Germany
[4] Helmholtz-Institut Mainz, Mainz, Germany
[5] Department of Physics, Johannes Gutenberg University, Mainz, Germany
[6] Laboratory of Powder Technology, École Polytechnique Fédérale de Lausanne (EPFL), Lausanne, Switzerland
[7] Department of Physics, University of Gothenburg, Gothenburg, Sweden
[8] present address: FRIB, 640 S. Shaw Lane, East Lansing, MI 48824, USA
[9] present address: SCK CEN, Boeretang 200, 2400 Mol, Belgium

Abstract We introduce a novel thick-target concept tailored to the extraction of refractory 4d and 5d transition metal radionuclides of molybdenum, technetium, ruthenium and tungsten for radioactive ion beam production. Despite the more than 60-year old history of thick-target ISOL mass-separation facilities like ISOLDE, the extraction of these most refractory elements as radioactive ion beam has so far not been successful. In ordinary thick ISOL targets, their radioisotopes produced in the target are stopped within the condensed target material. Here, we present a concept which overcomes limitations associated with this method. We exploit the recoil momentum of nuclear reaction products for their release from the solid target material. They are thermalized in a carbon monoxide-containing atmosphere, in which volatile carbonyl complexes form readily at ambient temperature and pressure. This compound serves as volatile carrier for transport to the ion source. Excess carbon monoxide is removed by cryogenic gas separation to enable low pressures in the source region, in which the species are ionized and hence made available for radioactive ion beam formation. The setup is operated in batch mode. Initially, we investigate the feasibility of the approach with isotopes of more than 35s half-life. At the cost of reduced efficiency, the concept could also be applied to isotopes with half-lives of at least one to 10s. We report parameter studies of the key processes of the method, which validate this concept and which define the parameters for the setup. This would allow for the

first time the extraction of radioactive molybdenum, tungsten and several other transition metals at thick-target ISOL facilities.

1 Introduction

The Isotope mass Separation OnLine (ISOL) technique was used already in 1951 to extract radioactive krypton isotopes from a 10 kg uranium oxide target, which was placed between the coils of a cyclotron magnet and irradiated by neutrons. The direct connection of the target to an ion source allowed simultaneous production and extraction of volatile species, and is today considered as the birth of the ISOL technique [1,2]. Modern ISOL targets use less material (see Ref. [3] for a recent review), but their areal densities are typically above several g/cm². The thick target is both a blessing and a curse: the number of radioactive atoms produced inside the target scales with its thickness, translating into high yields for volatile elements like mercury. At CERN-ISOLDE, which is supplied by 1.4 GeV protons from the Proton Synchrotron Booster (PSB), extractable yields for ^{197}Hg from a molten lead-bismuth target have been measured to be as high as 5×10^9 ions per µC of protons, while the mean proton current for molten targets can reach up to 1.5 µA [4–6].

Issues arise, if (i) the desired element is either chemically reactive and forms strong bonds to the target or to structural materials of the target and ion source system, (ii) the diffusion of the element in the target material is slow, or (iii) if the

ᵃ e-mail: jochen.ballof@cern.ch (corresponding author)

ᵇ e-mail: thierry.stora@cern.ch

effusion through open space from the target to the ion source is hindered due to long sticking times at each wall encounter. The mean sojourn time τ for a single wall collision can be estimated by the Frenkel equation [10,11],

$$\tau = \tau_0 \, e^{-\Delta H_{ads}/(RT)}, \qquad (1)$$

where R is the universal gas constant, τ_0 the period of vibration perpendicular to the surface in the adsorbed state and ΔH_{ads} the enthalpy of adsorption, which is a measure of the interaction strength between a single atom, molecule or ion and a surface. Hence, τ_0 is a property of the adsorbent only, while ΔH_{ads} depends on adsorbent and adsorbate. The latter can often be correlated to the macroscopic sublimation enthalpy of the adsorbent, characterizing the interaction between atoms or molecules of the same kind, which in turn is related to the vapour pressure of the compound. Hence, the vapour pressure is a measure for the mobility of a species during effusion processes for a given surface [12]. As can be seen from Eq. 1, the mean sojourn time depends exponentially on the temperature. Elements suffering from low vapour pressure and high boiling point are called refractory, and their extraction as ISOL beam provides a substential challenge. Volatile carrier molecules need to be formed, to enable transport of these elements to the ion source. From there they are either extracted as a molecular or even elemental ion beam, due to dissociation in the ion source. The process is called *in-situ* volatilization, chemical evaporation or extraction as molecular sideband. Reviews by Köster et al. give an excellent overview of the method and its limitations [13,14]. A recent development, not yet listed therein, is the successful extraction of the refractory and chemically reactive element boron as fluoride [15]. The elements for which short-lived isotope beams ($T_{1/2} < 1h$) are available from thick-target ISOL facilities are shown in Fig. 1. The most volatile elements, like noble gases, can already be extracted

Fig. 1 Periodic table of elements showing available and not yet available thick-target ISOLDE-beams of short-lived isotopes ($T_{1/2} < 1h$), in comparison with the elements forming carbonyl compounds [7–9]. S, Se and Te form compounds of type XCO (X= S, Se, Te), analogous to CO_2. Only the first six rows of the periodic table rows are shown

at low target temperatures. As both the sticking times and the diffusion processes inside the target material depend exponentially on the temperature, it is possible to extract most of the elements with the ISOL technique, if the target is operated at elevated temperatures. Therefore, the ISOLDE target container is made of tantalum and is designed to be heated restively to a maximum temperature of ca. 2250 °C.

As illustrated in Fig. 1, many transition metals are not yet available as ISOL radioactive ion beam. This region of the periodic table contains the most refractory elements like molybdenum, technetium, ruthenium and tungsten. These are at the same time the construction materials of the typical target and ion source unit. So far, it was only possible to extract tantalum as TaF_5 [9,16], which is compatible with the structural materials of a FEBIAD ion source. Long-lived ^{99m}Tc ($T_{1/2} = 6h$) could be extracted in elemental form from a tantalum carbide target equipped with a hot rhenium cavity by resonant laser ionisation. The online extraction of short-lived Tc isotopes is not reported [17]. Suitable sidebands for the remaining 4d and 5d refractory metals have not yet been found.

The requirements for volatile carriers are multifold. The compound should form easily upon reaction of a produced radioactive atom and a reaction partner, which is either present in the target and ion source system or introduced via injection of reactive gases. The latter can be either directly injected into the target or produced *in-situ* by heating a small solid sample which is connected to the target via a tube.

After formation of the isotope carrier compound, it has to travel from the target container via a transfer line to the ion source. On its way numerous wall encounters occur. Hence, the compound must be chemically inert towards the materials present in the target and ion source system. High temperatures are often beneficial for fast diffusion and volatile compound formation. However, it can be adverse to the desired chemical stability of the carrier molecule. This is especially the case, if decomposition is favored by thermodynamics, but could be inhibited kinetically, *i.e.*, by slower reaction rates at lower temperatures. Moreover, if decomposition is required for beam purification purposes, catalytic processes at low temperatures can be considered.

After eventually reaching the ion source, the compound needs to be ionized efficiently. For the extraction of the 4d and 5d transition metals of groups 6 to 9, which the present article is addressing, the extraction as fluoride or oxide has been discussed [9,13,16]. Both compound classes suffer from limited compatibility with the materials present in target and ion sources. This especially holds for tantalum, which forms strong bonds to oxygen and fluorine, thus decomposing the volatilized oxygen or fluorine-containing molecules upon impact.

Another issue arises from the target material. Typically uranium carbide targets are used at ISOLDE to produce heavy

elements, fission products and light neutron-rich fragments. The reductive environment and the presence of carbon in the material are adverse to oxidation reactions. The material structure of uranium oxide has only limited thermal stability and is prone to fast sintering, which increases the diffusion time. To follow a classical approach for the extraction of the refractory metal beams, the development of a new target material, ideally a target and transfer line free from metallic surfaces, and the integration of an efficient ECR (Electron Cyclotron Resonance) ion source would be required, due to catalytic decomposition of the volatile carrier on metallic surfaces and the given source temperatures. However, even after the implementation of all of these developments, the issue of slow diffusion in the target material remains. Hence, we propose a new target concept to bypass the limitations of a more classical high-temperature approach.

2 The target concept

To overcome operation at high temperatures, a novel target concept is proposed, allowing target operation at ambient temperature and pressure. The new concept aims at producing and extracting radioisotopes with half-lives of at least one to ten seconds in a batch-mode.

The recoil momentum allows ejectils of nuclear reactions to propagate through and emerge from thin metallic foils. In the proposed concept, the recoils are thermalized in a reactive gas and form volatile compounds *in-situ* (cf. Fig. 2). A compound class that appears well suited for *in-situ* volatilization is that of metal carbonyl complexes. As can be seen in Fig. 1, nine out of fifteen transition metals, of which beams are not yet available, form volatile carbonyl compounds. Already in 1961, the extraction of molybdenum from uranium oxide by formation of a volatile carbonyl compound was demonstrated [18]. Baumgärtner and Reichhold irradiated a mixture of U_3O_8 and $Cr(CO)_6$ with neutrons and were able to extract molybdenum hexacarbonyl by sublimation. Later, nuclear reaction products where thermalized in a chromium hexacarbonyl catcher, from which they could be evaporated as carbonyl compound [19]. However, a catcher made of $Cr(CO)_6$ is incompatible with an ion source as used in ISOL target units, due to its high volatility [20]. Recently, it was shown by Even et al. that volatile carbonyl complexes readily form at ambient temperature and pressure by thermalizing fission fragments of suitable elements in a carbon monoxide containing atmosphere [21,22]. Within our concept, the formation of the volatile compound is followed by removal of the reactive gas by cryogenic gas separation [23], as illustrated in Fig. 2b. The system is evacuated while the carbonyl compounds are retained in a cooling trap.

After excess gas removal, the cooling trap is allowed to warm up to release the volatile compounds, which are then fed into the ion source and ionized in collisions with electrons. In the following sections, the feasibility of the concept is investigated by means of proof-of-principle experiments of individual steps of the full procedure and numerical simulations. Molybdenum and tungsten were used as model case for the studies.

Despite their potential as volatile carriers, transition metal carbonyl complexes are delicate compounds, and decomposition in beam-induced plasmas and at elevated temperatures is expected [24–27]. In addition, impurities (*e.g.* oxygen or humidity) in the reactive gas reduce the chemical yield [28].

The topics addressed in the following sections aim at an order-of-magnitude estimation of radioactive ion beam yields that could be achieved. The average expected radioactive ion beam yield N computes to

$$N = N_0^{\text{batch}} \times \epsilon \times \nu_{\text{batch}}, \text{ where}$$
$$N_0^{\text{batch}} = \frac{I_p \, N_0}{\lambda} \left[1 - e^{-\lambda \, t_{\text{irr}}} \right], \text{ and} \quad (2)$$
$$\epsilon = \epsilon_{\text{extr}} \times \epsilon_{\text{stop}} \times \epsilon_{\text{form}} \times \epsilon_{\text{sep}}(\lambda) \times \epsilon_{\text{ion}}, \text{ with}$$

the in-target production yield by nuclear reactions N_0, the fraction of isotopes propagating through foils ϵ_{extr}, and of those stopped in the gas ϵ_{stop}, the formation of the volatile carrier molecule ϵ_{form}, the conditions required for removal of excess carbon monoxide gas and the associated efficiency ϵ_{sep} as well as the ionization efficiency of carbonyl complexes ϵ_{ion}. The number of isotopes N_0^{batch} with radioactive decay constant λ is produced per batch within the irradiation time t_{irr} at steady proton current I_p. The repetition frequency of the batch operation is ν_{batch}. Decay during separation is included in the efficiency factor $\epsilon_{\text{sep}}(\lambda)$. In the following sections, each parameter is explained and its numerical value is studied in detail. The considerations are based on the target concept shown in Fig. 2 and target geometries listed in Table 1.

The implementation at ISOLDE can be achieved with two different approaches. Standard target units already combine a class of target material, some chromatography setup and an ion source [29]. Following this approach, a compact setup is mandatory that is also suitable to operate in strong radiation fields. The dimensions and weight of the setup are limited by the maximum permitted load for the robot operating the target unit and the design of the target stations. Due to the low temperatures required for gas separation, needs arise to either implement a cryostat system at the target stations, or follow an alternative strategy for gas separation.

The second approach splits the setup in two assemblies. The gas-filled target remains installed at the target station, while the chromatographic setup is installed remotely, *e.g.* in the ISOLDE experimental hall. The carbonyl compounds are extracted as neutrals in a carbon monoxide stream to the remote location, which is an efficient and established technique, commonly used in transactinide synthesis to transport
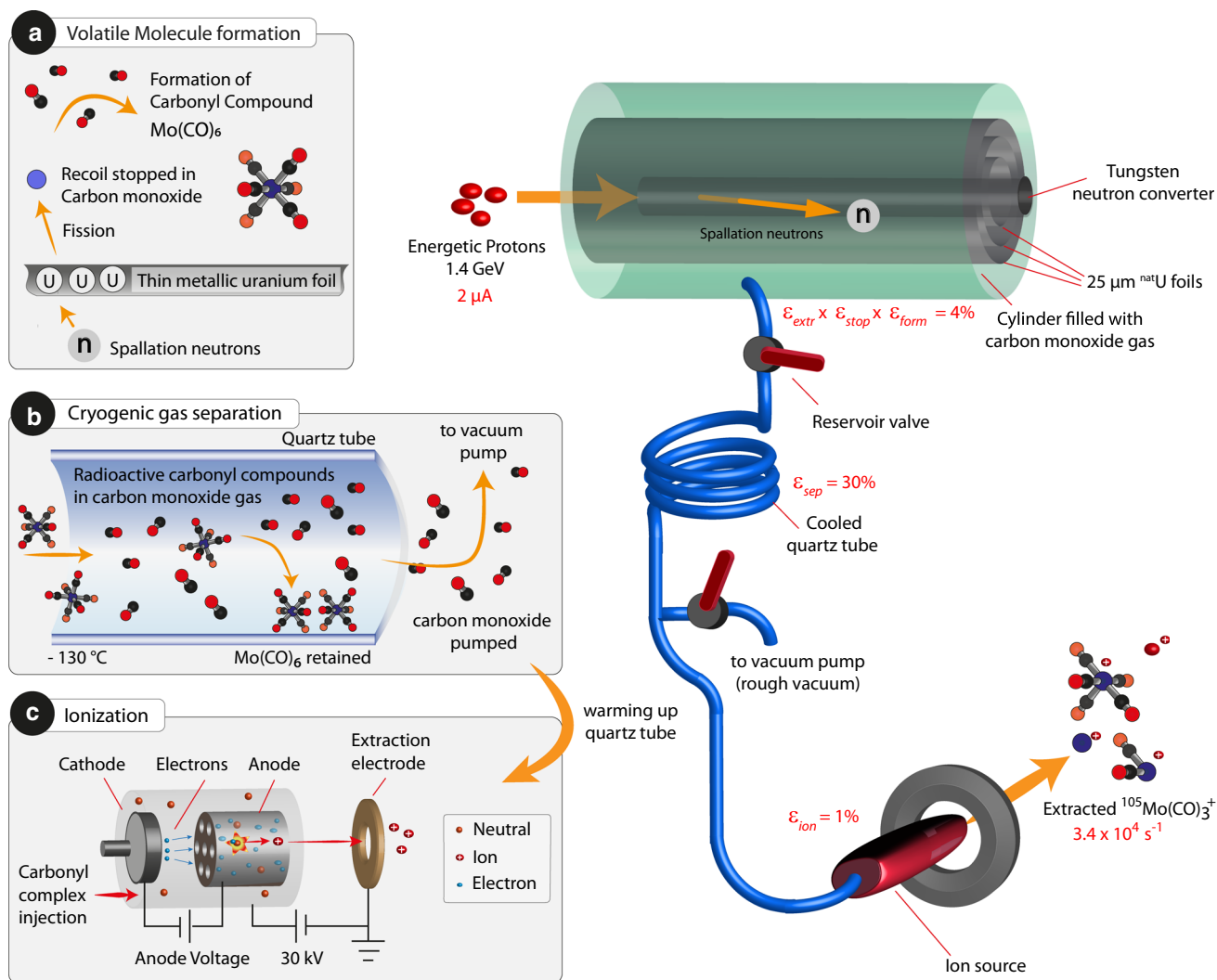
Fig. 2 Target concept for the extraction of refractory transition metals from a metallic foil target, shown exemplarily for the extraction of ^{105}Mo from uranium foils. Highly energetic protons impinge on a tungsten neutron converter and produce spallation neutrons. **a** The neutrons induce fission in the uranium foils and fission recoils emerge from the foil and are thermalized in carbon monoxide. Upon thermalization molybdenum hexacarbonyl complexes form readily. **b** The excess carbon monoxide is removed by retaining the carbonyl complexes on a cooled quartz surface and evacuation of the setup. After evacuation, the cooling trap is allowed to warm up to release the volatile compounds into the ion source. **c** Electron impact ionization is proposed to ionize molybdenum hexacarbonyl. Electrons emerging from a cathode are accelerated through a grid into a cylindrical anode where ionization takes place in collisions between neutral molecules and electrons. The ion source is kept at a potential of +30 kV and ions are extracted through the grounded extraction electrode. Further details are given in the text

the compound over a distance of several meters in short times [30]. The split installation circumvents size and weight limitations of the chromatographic setup and the operation of the latter in radiation environments.

2.1 In-target production

Direct exposure of a gas-filled chamber to an intense ion beam causes ionizing conditions which are expected to prevent carbonyl complex formation [31]. However, the high neutron fluences present in nuclear reactors do not hamper efficient carbonyl complex formation [21]. In addition, an intense ion beam passing a gas-filled chamber in the vicinity of the region of carbonyl formation does also not prevent carbonyl complex formation [32]. To avoid direct exposure to the intense proton beam, a spallation neutron source made of tungsten is proposed in our model setup. The latter is commonly found in ISOLDE target units and called proton-to-neutron converter [33–35]. This converter is concentrically surrounded by uranium or platinum target foils, which are placed inside a carbon monoxide-containing vessel. High production rates for molybendum and other 4d transition met-
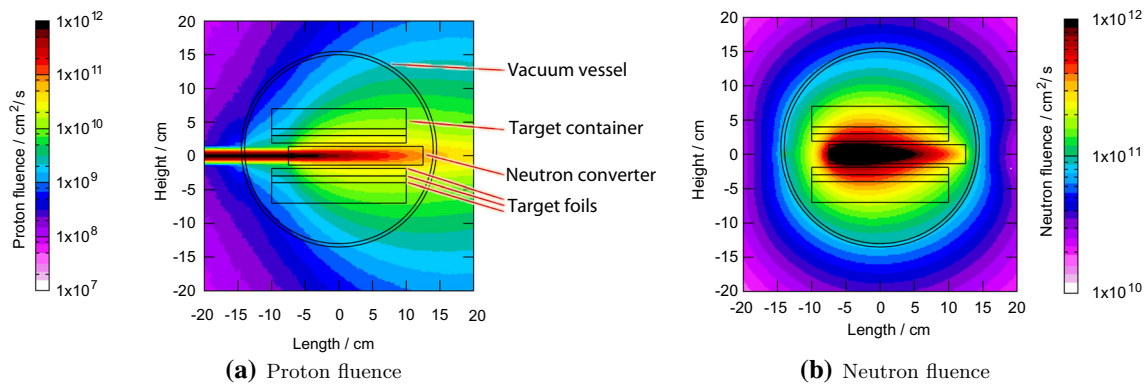
Fig. 3 **a** Proton and **b** neutron fluences at irradiation with 1×10^{13} protons per second obtained by FLUKA for the uranium foil geometry described in the text. The proton beam arrives from the left on the neutron converter. A sketch of the target is shown in Fig. 2

als are expected from uranium fission. Platinum was chosen because high production rates of tungsten are expected in spallation reactions.

Relative to the 20 cm-long foils, the converter is indented by 2.5 cm in the beam axis and direction. This layout is initially proposed to reduce the proton fluence in the target container, which emerges by scattering of the primary beam on the neutron converter [36–38]. The geometry parameters are listed in Table 1, and chosen under consideration of typical ISOLDE target size limitations and recoil ranges, but without further optimization, which is out of the scope of this conceptual work. The geometry could be further optimized (*e.g.* towards higher production rates and lower energy deposition on the tungsten rod) depending on the outcome of experiments studying carbonyl decomposition in such a setup. The power deposited by the primary proton beam might require modification of the geometry or the development of a dedicated cooling concept to avoid heating of the gas-volume to temperatures above the decomposition threshold for transition metal carbonyl complexes.[1]

The foil thickness was chosen based on expected recoil range and commercial availability.

As will be discussed in Sect. 2.2, the recoil energy of tungsten isotopes obtained in spallation reactions is lower than that of uranium fission products. Thus, a dense arrangement of thin (2 μm) platinum foils is desired. While the design is mechanically challenging, dense foil arrangements have already been realized by either using dimpled foils or dedicated spacers between the layers [39]. The proposed quantity of platinum foils (26 m^2) might be cost-prohibitive or require a custom manufacturing process. Further investigations towards a different type of platinum-containing material, *e.g.* films deposited on backing foils [40], could be sub-

ject of further studies. The replacement of platinum foils by gold foils could equally be considered.

The number of desired isotopes produced inside the target material per μC of primary beam N_0 was investigated with the FLUKA particle tracking code [41,42]. The 1.4 GeV proton beam was assumed to have a Gaussian profile with $\sigma = 0.35$ cm, which is the common irradiation mode for an ISOLDE proton beam focused on the target container. The resulting proton and neutron fluences are shown in Fig. 3. Due to scattering of the high energy proton beam on the converter, the beam broadens to form a plume. Using the proton-to-neutron converter reduces the proton fluence in the region of the gas-filled container by two orders of magnitude, in comparison to direct proton irradiation. The neutrons emerge isotropically from the tungsten rod. Overall, the uranium foils are exposed to a neutron fluence exceeding 2×10^{11} cm^{-2} s^{-1}, if the neutron converter is bombarded with 2.0 μA of protons. Figure 4 shows the in-target production yield of molybdenum and rhodium as 4d elements, and tungsten as 5d element. The latter figure contains simulation results for two different target materials and geometries, which are summarized in Table 1.

The in-target yields for molybdenum in the U(n,f) reaction reach a maximum for ^{105}Mo ($T_{1/2} = 36 s$) and decrease towards heavier and lighter isotopes. The yields on the outermost of the three foils are somewhat reduced due to the lower solid angle coverage and particle fluences. The yields of ^{105}Mo compute to 1.4×10^8 μC^{-1} for the innermost foil, 1.3×10^8 μC^{-1} (middle foil) and 1.1×10^8 μC^{-1} (outermost foil), reaching a total yield of 3.8×10^8 μC^{-1}. For comparison, the in-target production of ^{105}Mo in a typical uranium carbide target at ISOLDE (ca. 50 g cm^2 of ^{238}U), irradiated directly with the proton beam, is computed to 5.4×10^9 μC^{-1} by FLUKA [8].

The yields of the heavier element rhodium are in the same order of magnitude as molybdenum yields. The maximum yield of the tungsten isotopic chain in the Pt(n,spall) reaction,

---

[1] More recent simulations conducted for the design of an irradiation experiment (see Sect. 4) indicate that a converter length of 9 cm is sufficient and would significantly reduce the power deposition
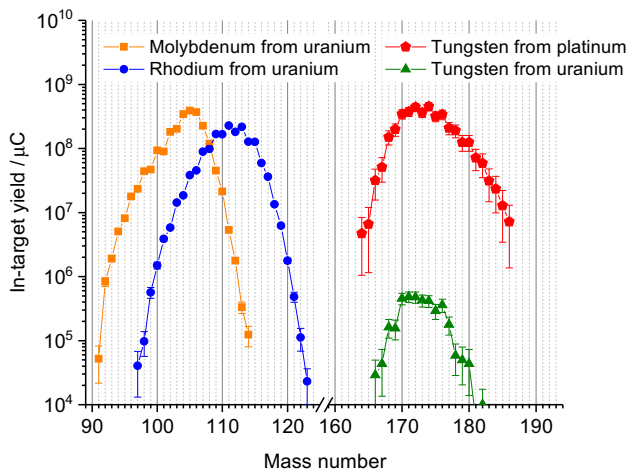
Fig. 4 In-target production for selected elements obtained by FLUKA. The error bars correspond to statistical errors of the simulation. The target geometry parameters are listed in Table 1

is found near ^{174}W. The total yield of this isotope produced in the platinum foil assembly is predicted to be $4.5 \times 10^8 \, \mu C^{-1}$.

2.2 Recoil range, thermalization and molecule formation

After production, the radionuclide propagates through the target material foil. Subsequently, it is crucial to thermalize the hot reaction products in the surrounding gas atmosphere to avoid implantation into the next foil or the container. The projected ranges in the respective materials depend on the kinetic energy of the recoil ion, which in turn depends on the underlying nuclear reaction, and the associated kinetic energy of the projectile. In addition, the projected range decreases with carbon monoxide pressure in the target container. In the following a pressure of 1bar (abs.) inside the target container, and a pure carbon monoxide atmosphere are assumed. These parameters were chosen due to the linear dependence of chemical yield on the volume percentage of carbon monoxide in the gas mixture [21] and the recoil range.

Protons and neutrons have been considered as projectiles inducing nuclear reactions, and their fluences in the target foils were obtained with FLUKA. Other secondary reaction channels are typically negligible and are not considered in in-target production simulations [43]. Folding the computed energy-differential projectile fluences with cross sections for isotope production computed by different codes, allows to identify the predominant reaction channel and finally, its associated recoil energy. For the low energy part (below 200 MeV.) of the incident particle spectra, TALYS [44,45] and GEF [46,47] were used. Higher energies were addressed with the ABRABLA code [48]. The energy distribution of spallation neutrons originating from a neutron converter in similar geometry has already been experimentally investigated and is in agreement with FLUKA simulations [34]. The cross sections given by ABRABLA have also been benchmarked with experimental results obtained at ISOLDE [43,49].

The neutron energy spectra obtained within this work follow a broad distribution with a maximum at ca. 3 MeV (evaporation neutron peak) and extend to ca. 1.4 GeV, which is the energy of the incident proton [50]. The spectra of protons have a maximum at ca. 100 MeV, and also extend to 1.4 GeV.

From simulations with the GEF code in the energy range from 100 keV to 20 MeV. for incident neutrons impinging on a ^{238}U target, the mean kinetic energy of ^{105}Mo fission recoils is expected to be between 90 and 100 MeV. ABRABLA equally predicts a recoil energy of ca. 90 MeV for 100 MeV neutrons. Excitation functions for the production of ^{174}W from ^{195}Pt have been calculated and folded with the proton and neutron fluence spectra. Incident particles from ca. 100 MeV. on significantly contribute to tungsten production. In total, the contribution of protons and neutrons to the production of ^{174}W, computes to 59% and 41%, respectively. The distribution maximum for the recoil energy of ^{174}W is near 1 MeV. It exhibits an exponentially decreasing tail towards higher energies.

The recoil ranges in the target foils and carbon monoxide gas have been calculated with SRIM [51,52] and fitted

Table 1 Assumed target foil geometries for in-target production and extraction efficiencies

	Unit	Uranium foils	Platinum foils
Converter radius	cm	1.4	
Converter length	cm	20.0	
Target container radius	cm	7.0	
Number of foils		3	483
Thickness	μm	25	2.5
Length	cm	20	20
Radii	cm	1.9, 3.0, 4.0	1.90 to 6.73
Total surface area	m^2	0.11	26.1

A sketch is shown as part of Fig. 2

with a polynomial function. The results for molybdenum in uranium foils indicate that a [105]Mo fission fragment has a range of ca. 6 mm in a metallic uranium foil. The range of a fission fragment emerging from the uranium foil in carbon monoxide depends on its energy after it emerges from the foil. To account for energy losses in the uranium foil and the target geometry, Monte-Carlo simulations were performed. Energy losses in the foil have been estimated by inversion of the obtained range function.

The simulation results predict that for commercially available uranium foils of 25 mm, in total $\epsilon_{extr}^{Mo} = 10\%$ of all [105]Mo fission recoils emerge from the foil. For comparison, a released fraction of 22% from an uranium oxide target at 1140 °C within 60 min was reported for Mo [53]. Release data at higher temperatures, as they are standard for uranium carbide targets, are not available and also difficult to predict due to the susceptibility of uranium oxide targets to undergo sintering.

The remaining recoil energy after propagating through the foil and the free flight path till the next surface determine if the recoil is thermalized in the gas or lost, due to implantation in a solid. The simulation predicts that $\epsilon_{stop}^{Mo} = 49\%$ of the emerging fragments are thermalized in carbon monoxide gas at 1 bar (abs.), leading to about 5% of all produced [105]Mo fragments being thermalized in gas. The bulk target material could be reduced by integration of thinner foils of *e.g.* 10 μm thickness, which would not decrease the total yield. Within the geometry assumed for platinum foils, $\epsilon_{extr}^{W} = 1.6\%$ emerge from the foil and thereof $\epsilon_{stop}^{W} = 21\%$ are thermalized in the gas.

After thermalization of the recoils in carbon monoxide gas, the carbonyl compounds form readily. Measurements have shown that in gas mixtures with inert gases, the chemical yield increases with the partial pressure of carbon monoxide. Using pure carbon monoxide gas, the chemical efficiency ϵ_{form} was found to be ca. 80% for the formation of Mo(CO)$_6$ and 30% for W(CO)$_6$ [21].[2]

2.3 Gas separation

A carbon monoxide partial pressure of 1 bar (abs.) inside the target container is desirable to achieve a high chemical yield, and is also crucial for efficient stopping of the fission recoils. However, ion sources typically operate under high vacuum conditions, and often a pressure of 1e-3 mbar may already prevent efficient ionization. Thus, the separation of radioactive carbonyl compounds from the excess gas atmosphere is required. Since carbon monoxide, exhibiting a boiling point of −191 °C [54], is by far more volatile than

carbonyl compounds, the two components are separable by chromatography. The implementation of a suitable cryogenic trap coupled to an ion source was already evaluated for the transport of carbon monoxide in a carrier gas by Powell et al. [55], and Katagiri et al. have also shown the feasibility of the integration into the process of radioactive ion beam production [23]. The option of neutral CO injection via a cryogenic trap into an electron-beam ion source for charge breeding is also considered for medical applications [56–58].

Adsorption enthalpies of carbonyl compounds have been measured on SiO$_2$, gold, Fluorinated Ethylene Propylene (FEP) and PolyTetraFluoroEthylene (PTFE) surfaces by isothermal chromatography and by thermochromatography [27,59–62]. In isothermal studies with radiotracers formed in the [249]Cf(n,f) reaction, an adsorption enthalpy for Mo(CO)$_6$ on SiO$_2$ surfaces of $-\Delta H_{ads} = 42.5(25)\,\mathrm{kJ\,mol^{-1}}$ was determined [21]. In thermochromatography experiments, the same quantity was found to be $-\Delta H_{ads} = 36(8)\,\mathrm{kJ\,mol^{-1}}$. Later experiments by Wang et al. reported values in agreement with earlier findings. Adsorption enthalpies of other transition metal carbonyl complexes (technetium, tungsten, rhenium, osmium, iridium) could also be deduced, all ranging in the same order of magnitude and indicating a physisorption interaction. For the following considerations, Mo(CO)$_6$ was chosen as a model case, and an adsorption enthalpy of -40 kJ mol^{-1} was assumed as average value of the measurements.

The system for cryogenic gas separation must be designed such that the total gas flow rate into the ion source does not exceed its maximum acceptable gas load and the pumping capacity of the vacuum system. A typical upper limit of 1×10^{-3} mbar L s^{-1} was estimated for gas injection into an ion sources operated at ISOLDE. In addition, the time needed to reach this condition should be as low as possible to minimize decay losses. The proposed setup is shown in Fig. 2b, which is operated in a batch-mode. A schematic flow diagram is shown in Fig. 6. During irradiation, the target container is filled with carbon monoxide at atmospheric pressure. After a defined irradiation time, which depends on the half-life of the desired isotope, the gas inventory is pumped by a roughing pump through a cooled quartz tube which retains the less volatile carbonyl compounds. After a certain fraction is evacuated from the target container, the latter is isolated from the chromatographic system by closing the reservoir valve. The residual pressure in the chromatographic tube is further reduced, till the maximum acceptable flow rate into the ion source is reached. Finally, the quartz tube is heated by a resistive heating element to a temperature that is sufficiently high to release the carbonyl compounds. The latter effuse into ion source, where they are ionized and electrostatically extracted. In parallel to the heating of the quartz tube, the irradiation of the next batch can take place, so that the heating period is not included in the cycle time ν_{batch}^{-1} of

---

[2] The given efficiency for molybdenum was obtained as ratio between transport by carbonyl formation and aerosol transport of atomic species attached to clusters. An absolute efficiency is given for tungsten.
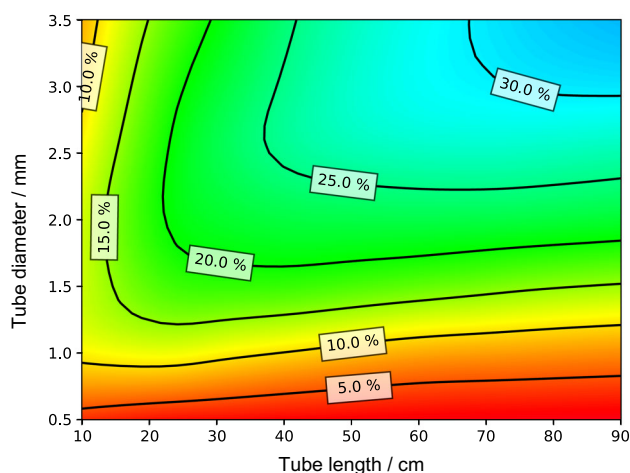
Fig. 5 Combined efficiency of excess gas removal and consideration of losses due to irreversible processes (like decomposition) for different dimensions of the chromatographic tube. The efficiency of excess gas removal is dominated by decay losses. The figure shows interpolated data that was obtained by simulation (see text)
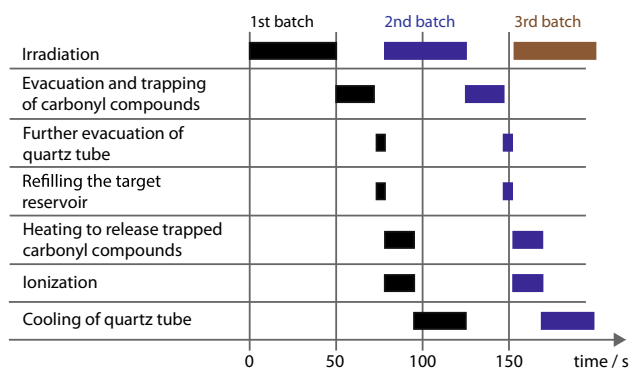

Fig. 6 Schematic flow chart of the batch process for the extraction of ^{105}Mo. Details are given in the text

the batch process. In the following, the separation efficiency ϵ_{sep} is estimated which is composed of (i) the efficiency of excess gas removal, (ii) decay losses occurring during the effusion of carbonyl complexes to the ion sources and (iii) further losses due to irreversible processes.

A Monte-Carlo model proposed by Zvara [63] was used to investigate the feasibility of the concept, which was also similar to the model used by Even et al. for the adsorption enthalpy measurements [59]. The model takes into account the temperature dependent sojourn times (cf. Eq. 1) and gas flow conditions. Assuming that the chromatographic tube is connected to an evacuated vessel (choked flow), the evaluation of Reynolds numbers for tube diameters from 0.5 to 3.5 mm suggests turbulent flow conditions.

The simulation generates particles with a random lifetime, which is sampled from a distribution according to the given half-life. Subsequently, the propagation of the particle through the chromatographic system is simulated. The length

of a displacement is typically approximated by the variance of the zone profile of the chromatographic peak, and expressions have been obtained for laminar flow *e.g.* Ref. [64]. Within this work, the mean length of a displacement was approximated by the diffusional deposition length in developed turbulent flow [65].

The efficiency of excess gas removal is given by a linear combination of (i) the fraction of carbonyl compounds evacuated from the reservoir (ii) the ratio of molecules which are inside the quartz column (*i.e.*, not decayed and not eluted) after the desired fraction was extracted from the reservoir, to the number of molecules fed into the column and (iii) an additional factor to account for decay losses during the time required to reach a flow rate below 10^{-3} mbar L s^{-1} which was estimated to be ca. 5 s. The input variables of the simulation were the fraction of carbonyl compounds extracted from the reservoir and fed into the quartz tube as well as its dimensions and temperature.

Quartz tubes with length and diameter of 10 to 90 cm and 0.5 to 3.5 mm, respectively, were considered. For each geometry of the separation channel, the respective highest excess gas removal efficiencies have been estimated by simulation. The simulation predicts that excess gas removal efficiencies above 60% are in reach for ^{105}Mo. Using the same geometry boundary conditions, the maximum excess gas removal efficiency for ^{108}Mo (1.11 s) is calculated to be above 0.6%. Typical temperatures are in the range of $-130(40)$ °C. Further details of the Monte-Carlo simulation are discussed in Ref. [66]. In addition to radioactive decay, irreversible sticking after decomposition or unwanted chemical reaction can lead to a further decrease of the gas separation efficiency. The extent of such additional losses can be estimated based on typical capillary transport losses, which could be in the order of 50% [22]. The combined efficiency of excess gas removal and consideration of losses due to irreversible processes is shown for ^{105}Mo in Fig. 5. At elevated flowrates, longer channels are required due to the increase in the diffusional deposition length.

After retaining the carbonyl complexes on the quartz tube and the removal of excess carbon monoxide, the temperature of the quartz tube is increased by resistive heating to allow the effusion of the carbonyl compounds towards the ion source. The transport time through an isothermal tube under molecular flow conditions can be estimated by the number of wall collisions, sojourn time per collision and the time spent in-flight. Equations have been summarised, *e.g.*, by Zvara in [65]. At a temperature of -30 °C, the transport time of ^{105}Mo(CO)$_6$ through an evacuated quartz tube of 3.5 mm diameter and 70 cm length computes to ca. 7s, whereof 2s arise from adsorption and 5s from time spent in non-adsorbed state. Fast heating can be achieved by using a metallic tube of high heat conductivity that is coated with SiO$_2$. A dedicated chromatographic setup needs to be designed and tailored to

the application, which is out of the scope of this conceptual work. Following heating times of commercial setups, the time required to raise the temperature from -140 to $-30\,°C$ is estimated to be in the order of 10 s. Thus, losses of ca. 28% need to be considered for the time required to feed the trapped carbonyl complexes of ^{105}Mo to the ion source. Thus, the total gas separation efficiency of ^{105}Mo computes to $\epsilon_{\mathrm{sep}}^{\mathrm{Mo}} = 22\%$. Decay losses for the long-lived isotope ^{174}W ($T_{1/2} = 31$ min) are negligible, and an efficiency of $\epsilon_{\mathrm{sep}}^{\mathrm{W}} = 50\%$ is assumed.

2.4 Ionization

A review about ion sources for radioactive ion beam production can be found in Ref. [67]. In contrast to ion sources designed to deliver stable isotope beams, additional requirements arise for the ionization of radionuclides. Due to their limited availability compared to stable isotopes, the ionization efficiency is one of the most important figures of merit. For exotic isotopes with very short half-lives ($\lesssim 100\,MS$), the residence time also needs to be considered. A compact design is required to meet constraints imposed by robot-handling of the target and ion source unit and resistance to the strong radiation field of the driver beam is mandatory.

The three main processes for ion generation are (i) surface ionization (ii) photo-induced ionization and (iii) electron-impact ionization. Surface ionization in hot cavities is applied for elements with low ionization potential (IP) of up to ca. 6eV like the alkaline or alkaline earth metals. For elements with elevated IP, resonant laser ionization can be used if laser systems are available to excite suitable transitions [68]. Electron impact ionization is the underlying process in electron beam (arc-discharge) ion sources and radio-frequency driven plasma ion sources. Via electron impact ionization, almost all elements and molecules can be ionized efficiently. Plasma sources are typically used for volatile species only.

The ionization of carbonyl compounds is a crucial step towards ion beam production. The method of ionization must be chosen carefully with respect to the properties of the compound. The ionization potential of $Mo(CO)_6$ was measured to be in the range from 8.2 eV to 8.5 eV [69–72]. The first bond dissociation energy (FBDE) is significantly lower and was determined to be 1.7 eV by pyrolysis with a pulsed CO_2-laser in a gas cell [73], in agreement with data obtained by thermal decomposition on a silver surface [24,25] and theoretical studies [74,75]. In comparison to typical candidates for molecular beams at ISOLDE, the compound is delicate, and decomposition on hot surfaces is expected. For species with high ionization potential, Forced Electron Beam Induced Arc-Discharge (FEBIAD) ion sources [76], like the VADIS (Versatile Arc-Discharge Ion Source) [77] are commonly used. However, the high operating tempera-

ture is expected to decompose the carbonyl compounds even before they reach the ion source volume. Thus, ion sources operated below decomposition temperature, favoring high electron energies for ionization and efficient ion extraction over breakup, are the preferred choice.

2.4.1 Arc-discharge ion sources

In arc-discharge ion sources, electrons are emitted from a cathode and accelerated to an energy of ca. 100 eV to 200 eV to enable electron impact ionization. The electrons are typically emitted thermionically. Arc-discharge ion sources, in contrast to compact radio-frequency plasma ion sources, offer the advantage of a narrow electron energy distribution and relatively high electron energies. The latter avoid favouring breakup over ionization due to insufficient electron energy. Thus, the application of electron impact ionization in a cold environment presents an interesting asset. Penescu et al. proposed Eq. 3 to model the ionization efficiency of FEBIAD-type ion sources [78]. The ionization efficiency ϵ_{ion} depends on the rate of ionization per unit volume R_{ioniz}, the volume of the ionization region V, the number of neutral particles injected per unit time n_{in} and an additional factor f to account for the probability of ion extraction, electron confinement and higher order effects. The rate of ionization can be expressed as a linear combination of the number densities of neutral particles N_n, electrons N_e, the ionization cross section σ and the relative velocity of electrons and neutral particles v_{el}.

$$\epsilon_{\mathrm{ion}} = \frac{R_{\mathrm{ioniz}} V}{n_{\mathrm{in}}} f, \quad \text{where} \quad R_{\mathrm{ioniz}} = N_n N_e \sigma v_{\mathrm{el}} \tag{3}$$

Unfortunately, absolute partial ionization cross sections for molybdenum hexacarbonyl or its fragments have not yet been published. It is interesting to note that also the ionization cross section of molybdenum has not yet been measured due to the refractory nature of the element and only theoretical calculations are available [79].

Due to the lack of available data, we conducted a comparative study of the ionization efficiency of the noble gas krypton and molybdenum hexacarbonyl in a cold environment. We chose to use a laser to liberate electrons out of the tantalum cathode of a standard VADIS source equipped with a water cooled transfer line (VD7). In contrast to common operation of the VADIS ion source, the source was not resistively heated. The laser pulses impinging on the cathode induce a local raise of temperature during the laser pulse. However, the heat is dissipated quickly to the water-cooled assembly [80]. The laser power used in our experiment is not expected to raise the average temperature of the cathode significantly. Thus, thermal decomposition of carbonyl compounds on the cathode is negligible.
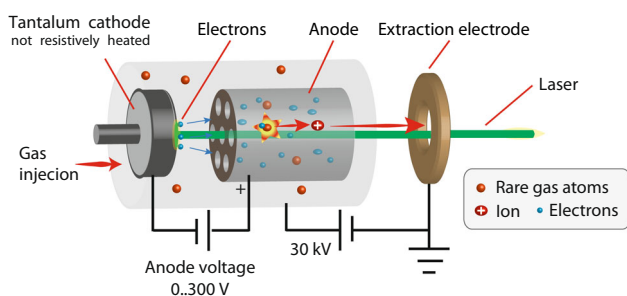
Fig. 7 Principle of the exploratory experiment exploiting electron generation by a laser beam in a cold environment. The electrons are liberated from the cathode and accelerated through a grid into the positively biased anode body, where volatile species are ionized in collisions

The candidate mechanisms for electron generation in the interaction of the laser beam and the tantalum cathode are either extraction from a plasma plume, thermionic electron emission or the photo-electric effect. As discussed in the next paragraph, the used fluences were most likely insufficient for ablation and plasma formation. Time-dependent heat transfer and thermionic electron emission models for tantalum are available [81], but require more precise knowledge of pulse fluence than available from our experiment to be applied. Since the single photon energies were below the material work function, the absorption of multiple photons is required to release electrons by the photo-electric effect. Efficient multiphoton photoemission has been observed with ultrashort ($\tau_p = 80\,fs$) laser pulses [82] but data on quantum efficiency are not available for the conditions present in our experiments. Nonetheless, in both scenarios electrons are extracted in an environment that is (on average) at ambient temperature.

Experimental

A sketch of the ion source is shown in Fig. 7. UV light (343 nm) supplied by a Light Conversion PHAROS PH1-15-0400-02-30 laser at 50 kHz repetition rate and pulse length of 265 fs was guided through the ion beam outlet aperture on the tantalum cathode. The laser power before entering the vacuum system was measured to be 4.5 W. The dimensions of the laser spot were estimated with the bare eye and measured to be ca. 5 mm in diameter. Due to the limited ion beam outlet aperture of only 1.5 mm in diameter, only a fraction of the beam power reached the cathode. An upper limit for the fluence per pulse computes to $\phi_l < 5 \times 10^{-3}\,\mathrm{J\,cm^{-2}}$[4].The minimum laser fluence needed for ablation (threshold fluence) was estimated in Ref. [83] to be 0.17 J cm^2 at $\lambda_l = 750\,\mathrm{nm}$ and a pulse length of $\tau_p = 8.5\,fs$. Thus, the source in our experiment was most likely not operated in an ablation regime.[3]

Table 2 Ionization efficiency estimation of the exploratory cold electron impact ion source shown in Fig. 7

Nuclide	Isotope abundance	Current	Injected neutrals	Ionization efficiency
^{98}Mo	24.3%	33 pA	2238 pnA	0.0015%
^{84}Kr	57.0%	200 pA	8999 pnA	0.0022%

The efficiency is given for the most abundant fragment of Mo(CO)$_6$, and corrected for isotope abundance. The aim of the experiment was to deduce the *relative* ionization efficiency of the two species

Krypton (Carbagas, 99.998%) and molybdenum hexacarbonyl (Schuchardt München, TA Mo 36.33%, C 27.18%, Fe 0.005%, Cu 0.0008%) were supplied through a common transfer line into the ion source. The krypton flow rate was controlled with a calibrated leak, which was measured to be 1.15×10^{-5} mbar L s^{-1} for 1bar (abs.) of helium. The setup for the controlled injection of molybdenum hexacarbonyl consisted of an evaporation chamber, connected to the common transfer line via a regulation valve (Pfeiffer EVR116). The evaporation chamber was equipped with a capacitance diaphragm gauge (Pfeiffer CMR 373) to monitor the pressure. The residual gas composition was monitored by a residual gas analyzer (Pfeiffer PrismaPlus) at the extraction site of the ion source.

After introduction of a solid Mo(CO)$_6$ sample into the evaporation chamber, the latter was evacuated with a turbomolecular pump, backed by a dry scroll pump, to a pressure below 1×10^{-2} mbar. Subsequently, the valve to the pumping group was closed. The sample quickly evaporates untill the saturation vapour pressure is reached inside the reservoir. Successive opening of the regulation valve allowed controlled injection into the transfer line. The material consumption was estimated by allowing the complete evaporation of a known amount, which was monitored via the pressure of the evaporation chamber and by the residual gas composition. The material consumption was measured to be $88^{+5}_{-21}\,\mu$ g h^{-1}. The relatively large error is due to consideration of material losses during the initial evacuation. The results of the relative efficiency measurement of Kr and Mo(CO)$_6$ are listed in Table 2 and an obtained mass spectrum is shown in Fig. 8. The ionization efficiencies of krypton and molybdenum compute to 0.0022% and 0.0015%, respectively. The result of the experiment shows that the ionization efficiencies of Kr and Mo(CO)$_6$ are in the same order of magnitude. While these ionization efficiencies in combination with high in-target production rates, or vaporization of a radioactive Mo(CO)$_6$ sample obtained by other means, would already allow a range of nuclear physics experiments, a higher efficiency is desirable.

---

[3] Attempts to further focus the laser beam with a telescope caused high voltage breakdowns and damage on the cathode surface. However, in

the experiments described in this work, the focusing telescope was not used.
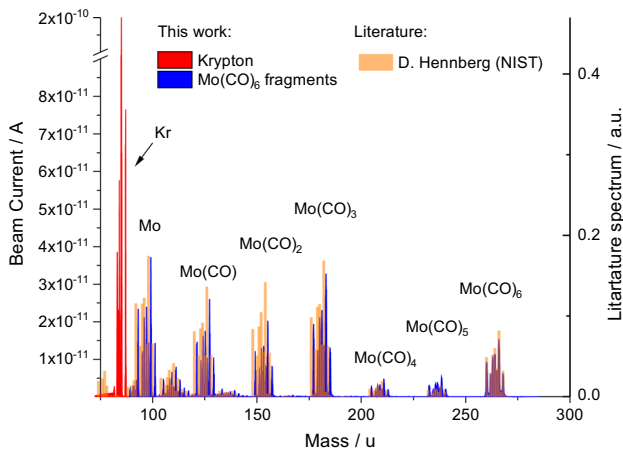
Fig. 8 Typical mass spectrum of Kr and $Mo(CO)_6$ measured simultaneously with the cold electron impact source. A mass spectrum of $Mo(CO)_6$ obtained also by electron impact ionization by Henning in [84] is shown for comparison. Minor deviations in the fragment distribution might arise from different electron energies or source characteristics

Proposed design of a cold photo-cathode driven ion source

in the following, we explore the feasibility of an electron-impact ion source exploiting the photo-electric effect for electron release.[4] Basic design parameters for a novel photo-cathode driven ion source will be derived that aims at an ionization efficiency of $\sim 1\%$ for $Mo(CO)_6$. First, the general assumptions are presented, then the space-charge limitations of an electron current passing through the gap between cathode and anode are discussed and finally the basic requirements of a suitable laser system are given.

The efficiency estimate of the new design is based on the assumption that the measured ionization efficiency obtained in our exploratory experiment scales linearly with the electron current. This is expected in a first approximation, since the rate of ionization linearly depends on the electron density. The probability of ion extraction, which is included besides other effects in the factor f of Eq. 3, is affected by source geometry. However, in contrast to the required increase of several orders of magnitude on the electron current, the extraction factor is typically only affected to some minor extent [78], which could be subject of further studies.

The electron currents in our experiment have been obtained as drain current of the anode power supply. However, the instantaneous currents might have exceeded acceptable values for the used pico-amperemeter. To avoid underestimating the electron current, which would lead to overestimation of the photo-cathode source efficiency, we assume

a space-charge limited current in following considerations. The measured electron currents were about factor two below the calculated space-charge limited current at a typical anode potential of 120 V. The observation of saturation effects of electron current with laser pulse energy might also indicate operation in proximity of a space-charge limited regime.

The maximum current density J_p that can pass a gap of length d_g with a potential difference of V_g is classically given by the Child–Langmuir law [87,88]. If the transition time of electrons between cathode and anode grid is long compared to the laser pulse of duration τ_p, a single sheet approximation can be applied [89]. Corrections for the two-dimensional geometry have been proposed in Ref. [90]. The maximum mean current I_m (without virtual cathode formation occurring) is given by

$$I_m = J_p \, \pi r_{em}^2 \, \xi \, \tau_p = \left(1 + \frac{d_g}{4 r_{em}}\right) \frac{\epsilon_0 \pi r_{em}^2 V_g}{d_g} \, \xi, \qquad (4)$$

where ξ is the pulse repetition rate and r_{em} the radius of the electron-emitting surface. To allow higher electron currents, the repetition rate of the laser or the diameter of the electron-emitting surface can be increased. Increasing the anode potential V_g would push the ionization cross section into an unfavorable regime, and the further reduction of anode-cathode distance (typically 1.5 mm) reduces the reliability of the ion source since a minor displacement is sufficient to cause an electrical contact between anode and cathode.[5]

The laser driver is most effective if the resulting electron pulse charge does not the exceed the critical limit $q_c = I_m \xi^{-1}$. The characteristic parameters, such as mean power P_l, pulse energy $E_l = P_l \xi^{-1}$ and pulse energy fluence $\phi_l = E_l \pi^{-1} r_{em}^{-2}$ can be estimated by the quantum efficiency ϵ_q, i.e. the ratio of emitted electrons to photons hitting the surface, as

$$E_l = \frac{h \, c}{\lambda_l} \frac{q_c}{\epsilon_q \, e}, \qquad (5)$$

where h is the Planck constant, and λ_l the photon wavelength. Many high-quantum-efficiency materials are semiconductors, like cesium telluride. They require sophisticated vacuum systems (pressures below e-9mbar) to reach their nominal performance [91]. On the other hand, metal cathodes have a lower quantum efficiency but can operate at higher pressures. Thus, a copper cathode was chosen for the estimations which has a quantum efficiency of ca. 0.014% at 266 nm and a residual pressure of 10^{-7} mbar [85,91].

A set of design parameters for a cold photo-cathode driven ion source and laser system is proposed in Table 2. Following the previous discussion, the parameters are chosen such that

---

[4] A more recent experiment has shown that an electron-impact ion source can be driven by a copper photo-cathode. In the latter experiment, we did not observe an impact of sputtering of the copper cathode on the ion source performance during several days of operation [86].

[5] Such issues were observed for resistively heated cathodes of VADIS at ISOLDE.

Table 3 Parameters of a proposed cold electron-impact ion source that exploits a photo-cathode as source of electrons and is expected to reach an ionization efficiency of 1% for $Mo(CO)_6$

Parameter	Symbol	Unit	Exploratory experiment	Proposed photo-cathode source
1. Geometry and calculated critical bunch charge				
Laser spot diameter[†]	$2r_{em}$	mm	1.5	12
Anode-cathode distance	d_g	mm	1.5	3
Critical bunch charge[§]	q_c	pC	2	45
2. Cathode and laser wavelength				
Cathode material			Ta	Cu
Center wavelength	λ_l	nm	343	257
Quantum efficiency at λ_l	ϵ_q	%	−[‡]	0.014 [85]
3. Required laser system				
Pulse repetition rate	ξ	MHz	0.05	2
Average power	P_l	W	< 4.5[‖]	3.7
Pulse energy	E_l	μJ	< 90[‖]	1.9[#]
Fluence per pulse	ϕ_l	$\mu J\,cm^{-2}$	< 5093[‖]	1.6
4. Calculated mean electron current and ionization efficiency				
Mean electron current	I_m	μA	0.09	90
Ionization efficiency	ϵ_{ion}	%	0.001	1

The ionization efficiency of the proposed source is estimated by scaling the measured ionization efficiency of $Mo(CO)_6$ obtained in an exploratory experiment by the respective calculated electron currents. In the experiment, electrons were liberated by a laser, however the exact mechanism of electron production could not be identified. The increase in electron current (*cf.* Eq. 4) can be achieved by adaptation of the geometry which allows higher bunch charges without virtual cathode formation and an increase in the repetition rate of the laser. An anode potential of $V_g = 120V$ is assumed. See text for details

[†] Circular area on the cathode that is illuminated and emits electrons

[§] Calculated maximum charge that can be transported in a short pulse between cathode and anode without virtual cathode formation

[‡] Data on multiphoton quantum efficiency not available and mechanism of electron production unclear

[‖] An upper limit is given based on the measured laser power before entering the vacuum system.

[#] Chosen to match critical charge q_c

an ionization efficiency of 1% for $Mo(CO)_6$ could be reached under the assumption that the measured ionization efficiency scales linearly with the space-charge-limited electron current. The proposed design assumes a laser spot diameter of $2r_{em} = 12\,mm$ which is equal to the size of the VADIS cathode. In our preparatory experiment (*c.f.* Fig. 7), the laser beam was guided through the ion beam outlet hole on the cathode. An increase of the outlet hole diameter from currently 1.5–12 mm might significantly decrease the source efficiency because it reduces the residence time of neutral species in the anode body. Thus, we propose to introduce the laser beam perpendicular to the electron beam, a trajectory that was recently developed for the perpendicularly-illuminated LIST ion source [92]. The aforementioned laser path is estimated to require an increased anode-cathode distance of ca. 3 mm. The required pulse energy fluence computes to 1.9 μJ cm^{-2} which is well below the ablation threshold of 0.77 J cm^{-2} even for short (10 fs) pulses [93]. Other factors contributing to damage of photo-cathodes have been identified. In Ref. [94], the damage threshold for copper photo cathodes was estimated by simulation and a fluence of less than 40 mJ cm^{-2} is recommended. The reliability and efficiency of such

a photo-cathode source might be impacted by condensation of molecule fragments on the cathode or the residual pressure of carbon monoxide. Its behavior needs to be experimentally verified.

A deep ultra violet (DUV) laser is required for efficient release of electrons from metal photo-cathodes. Due to the limited bunch charge, high repetition rates are beneficial. As listed in Table 2, the desired efficiency of ca. 1% for $Mo(CO)_6$ could be reached with 3.7 W average power at a wavelength of 257 nm and repetition rate of 2 MHz. A recent review about DUV laser generation is given in Ref. [95]. The required laser system could be based on fourth harmonic generation of a 1 μm Yb fiber laser. Besides pulsed lasers, also continuous wave (cw) lasers could be considered [96–98]. For the latter, additional considerations apply for ionization efficiency estimates, as will be discussed in the following paragraphs.

Continous thermionic source efficiency

The spatial separation of a resistively heated cathode and ionization volume provides an alternative path towards a cold electron impact ion source. A thermionic electron source could be placed remotely in an actively cooled environ-
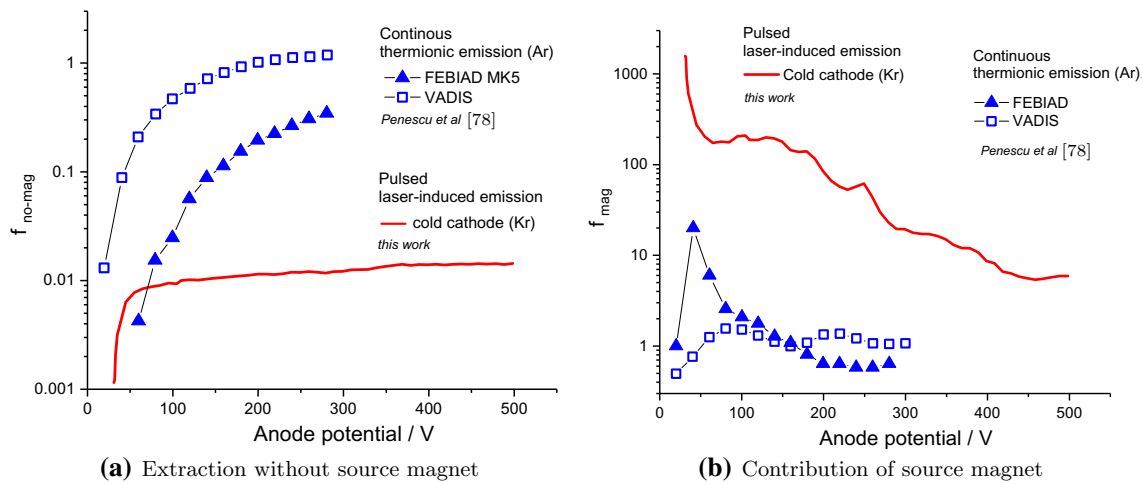
(a) Extraction without source magnet

(b) Contribution of source magnet

Fig. 9 Contributions to the extraction factor $f = f_{no-mag} \, f_{mag}$, according to Eq. 6, for the exploratory cold ion source shown in Fig. 7 used in this work, in comparison to data from FEBIAD sources, which were taken from [78]. The magnet currents in (**b**) were 4.5A and 6A for the continuous thermionic source and the pulsed laser-induced emission source, respectively. See text for details

ment, with no line of sight to the ionization volume to avoid radiative heating. The achievable ionization efficiencies of $Mo(CO)_6$ in such a configuration can be estimated from krypton efficiencies, which are in the range of 30% for known FEBIAD-type sources [76,77].

For this, our experimental results are compared to the aforementioned model (Eq. 3). While the ionization cross-section of a given compound is independent of the ion source, the extraction factors f of a continuously operated thermionic emission ion source and a pulsed laser-induced emission source are expected to differ, even if the geometry of the cavity is similar. In the first case, the continous release of electrons generates an electric field in the ionization volume which influences the extraction of ions. It was proposed that this is due to the formation of a potential well [77,99–101]. In comparison to the immediate extraction of a nascent ion guided by a favourable field, a potential well might also increase the number of wall collisions of an ion before extraction. The latter would decrease the extraction factor f, particularly for condensible species which are lost to surfaces upon collision. The pulsed electron generation in our experiments is expected to significantly reduce the aforementioned hindrance due to the limited life-time of electrons [78]. On the other hand, the electric field present in sources with continuous electron emission might guide produced ions towards the outlet. In an electron-free environment, the operation at room temperature contributes to a more efficient ion extraction. The field produced by the grounded extraction electrode penetrates into the anode volume and decreases the potential near the outlet aperture. Ions created in this region are guided along the decreasing field towards the outlet hole. To overcome the gradient to the outlet hole, a certain ion energy is required. Thus, as argued in Ref. [78], the region of

direct extraction (active volume) decreases with increasing ion energy.

By evaluation of the parameters given in Eq. 3 similar to the derivation discussed in [78], it can be written as

$$\epsilon_{ion} = \frac{I}{e \, S_{out}} \sqrt{\frac{2 \, \pi \, M}{R \, T}} \, \sigma \, l \, f, \qquad (6)$$

where I is the electron current, e the elementary charge, S_{out} the cross-sectional area of the outlet hole, T the temperature of the ion source, M the molar mass of the neutral species, R the universal gas constant, l the length of the ionization volume in the axial direction and σ the ionization cross-section. As in Eq. 3, the probability of ion extraction (and other effects) is solely included in the factor f. As already discussed, the electron current I was approximated with the theoretical space charge-limited current, estimated for short pulses [89] and corrected for the limited emitter surface [90].

The dependence of the extraction factor f on the anode potential is shown in Fig. 9 for krypton beams from the exploratory cold ion source (*cf*. Fig. 7) using evaluated cross sections [102], along with data obtained for argon from FEBIAD-type sources [78]. For this measurement, light at a wavelength of 515 nm was used. The extraction factor is given as linear combination $f = f_{no-mag} \, f_{mag}$. The factor f_{no-mag} is directly obtained from a measurement with disabled source magnet. The factor f_{mag} is calculated by dividing the extraction factor with enabled magnet by the previously obtained factor f_{no-mag}. As can be seen from Fig. 9, the similarity in the curves for pulsed laser-induced and continous thermionic electron emission indicates that in both cases electron impact ionization is observed. As discussed in more detail in Ref. [78], the factor f_{no-mag} increases with anode potential, which can be attributed to a reduced

space-charge repulsion at higher electron velocities leading to a better electron confinement. For FEBIAD-type sources, the ion extraction might also be favored at higher voltages due to a reduced Debye-length and increased active volume. The magnetic field increases the electron density, an effect which is significantly more pronounced for the laser-induced electron emission ion source. Deviations between the cold exploratory ion source and FEBIAD-type sources arise not only due to the laser induced, pulsed release of electrons, but also due to a different geometry of electron extraction. While the whole cathode surface (ca. 12 mm diameter) emits electrons in thermionic mode, the laser spot is defined by the diameter of the outlet aperture of the source, which is 1.5 mm only. Seeing the similar shape of the curves, an order-of-magnitude estimation of the extraction factor for the VADIS source in the ionization process of molybdenum hexacarbonyl is proposed in the following, provided the cathode heating and the ionization volume with the anode can be decoupled as already discussed.

Due to unknown ionization cross sections of $Mo(CO)_6$, the extraction factor f cannot be experimentally obtained from an efficiency measurement. However, the short lifetime of electrons after a laser pulse, in comparison to longer extraction times of ions, suggests that the hindrance of extraction by electrostatic fields inside the cold exploratory ion source is low. Thus, as first approximation it is assumed that the krypton extraction factor f_{Kr}^L is equal to the extraction factor of molybdenum hexacarbonyl $f_{Mo(CO)_6}^L$ in the cold exploratory ion source.[6] The situation in the VADIS source is different, and the extraction factor of $Mo(CO)_6$ is approximated with the extraction factor of carbon monoxide, which suffers from similar electron-beam induced decomposition issues as $Mo(CO)_6$ inside the source. Under these assumptions, the ionization efficiency of $Mo(CO)_6$ in a cavity with only cold surfaces (*i.e.* no thermal decomposition), computes to[7]

$$\mathcal{E}_{Mo(CO)_6}^{VD} \sim \mathcal{E}_{Mo(CO)_6}^{L} \frac{\mathcal{E}_{Kr}^{VD} f_{CO}^{VD}}{\mathcal{E}_{Kr}^{L} f_{Kr}^{VD}} \sim 2\%. \tag{7}$$

The ion source proposed here is exposed to a significant partial pressure of residual carbon monoxide. While in some cases results have been obtained which indicate that residual carbon monoxide might increase the ionization efficiency for elements with lower ionization potential [99], experimental results for molybdenum hexacarbonyl are not available.

---

[6] A mass dependence of the extraction factor has been observed, however even the ratio of xenon and argon extraction factors was found to only be $\frac{f_{Xe}^{VD}}{f_{Ar}^{VD}} \approx 1.8$ [78].

[7] The calculation assumes a typical ionization efficiency of 1% for carbon monoxide, an ionization cross section of ca. 1.9×10^{-20} m^2 at 120 V anode potential [103], space-charge limited electron current, and a distance between anode and cathode of 1.5mm.

A drawback of ion sources exploiting electron impact ionization is the lack of selectivity. Separation of isobaric contaminants in the radioactive ion beam has been achieved by element-dependent adsorption on quartz columns [29,104]. Unfortunately, this technique might not be suitable to separate carbonyl compounds from different elements, as their adsorption enthalpies are in the same range [30]. An alternative approach could be based on differences in compound stabilities. Carbonyl complexes of Tc, Ru and Rh readily decompose on gold surfaces already at ambient temperature (30–50 °C), whereas Mo complexes have a survival probability of 60% in the same setup [24]. Differences in the ionization fragmentation patterns could be exploited for additional selectivity.

2.4.2 Laser ionization

Resonant laser ionization is a powerful tool for element-selective ionization. However, the technique is typically only applied to single atoms. Recently, a resonant laser ionization scheme for molybdenum was developed and tested online at ISOLDE [106]. Exploiting this scheme for carbonyl compounds requires first to strip the molybdenum atom of its carbonyl ligands. Laser induced breakup of the compound [107,108] is widely discussed in literature and resonant breakup is also reported in Ref. [109]. The concept of laser-induced neutral dissociation followed by resonant laser ionization is further discussed in Ref. [110]. While the efficiency of laser induced breakup and ionization has not yet been quantified, the method would allow element-selective ionization.

3 Conclusions and implementation at ISOLDE

Within the previous sections, we have provided a concept for a gas-filled recoil target, which can be used at ISOL facilities. Thin metallic foils acting as target material are placed around a tungsten rod, which serves as a spallation neutron source. Instead of diffusion, the recoil energy of the reaction product is exploited to extract the radioisotopes from the foil. They are subsequently thermalized in carbon monoxide gas. Volatile carbonyl complexes form at ambient temperature and pressure. The carbonyl complexes are chromatographically separated from the carbon monoxide gas and fed into an ion source. Following the discussion in the previous section, the estimated efficiency for each step is listed in Table 4. Experimentally obtained ionization efficiencies in a proof-of-principle setup along with expected values after successful ion source development are given. In the former case, intensities in the order of 37 s^{-1} for ^{105}Mo from uranium foils and 6 s^{-1} for ^{174}W from platinum foils can be expected. After successful development of the proposed ion source, a

Table 4 Estimation of expected ion beam yields of ^{105}Mo from uranium foils, and ^{174}W from platinum foils

Symbol	Unit	Description	^{105}Mo		^{174}W		Ref.
$T_{1/2}$	s	Half life	36		1860		[105]
Predominant production reaction			U(n,f)		Pt(n,spall)		Sect. 2.1
N_0	$\times 10^8\,\mu C^{-1}$	In-target production	3.8×10^8		4.5×10^8		Sect. 2.1
t_{irr}	s	Irradiation time	50		400		Sect. 2
I_p	μA	Proton current	2.0		2.0		[5]
N_0^{batch}		Isotopes per batch	2.4×10^{10}		3.3×10^6		Eq. 2
ν_{batch}^{-1}	s	Cycle time	83		454		Sect. 2
ϵ_{extr}	%	Extraction eff.	10		1.6		Sect. 2.2
ϵ_{stop}	%	Stopping eff.	49		21		Sect. 2.2
ϵ_{form}	%	Chemical eff.	80		30		[21]
ϵ_{sep}	%	Gas-separation eff.	22		50		Sect. 2.3
ϵ_{ion}	%	Ionization eff. †	1	0.0015	1	0.0015	Sect. 2.4
N	s^{-1}	Average ion rate	2.5×10^4	37	3.9×10^3	6	Eq. 2

†Two ionization efficiencies are given. The lower efficiency was measured in an exploratory experiment with a cold VADIS, in which electrons were released by a laser. The higher efficiency is an estimated value that is believed to be in reach after development of a cold FEBIAD-type ion source (cf. Sect. 2.4)

total intensity of 2.5×10^4 s^{-1} for ^{105}Mo and 3.9×10^3 s^{-1} for ^{174}W is expected. Typically, intensities in this order of magnitude are compatible with post-acceleration within the HIE-ISOLDE linac [111].[8]

Presently, radioactive ion beams of 4d refractory elements are available from in-flight separation facilities like BigRIPS (Japan) and gas-cell facilities like IGISOL (Finland) and CARIBU (USA) [112]. For example, at BigRIPS beams of ^{105}Mo have been extracted [113]. Based on an observed production rate of 7.44×10^2 pnC^{-1} [114] and a typical ^{238}U primary beam current of 70 pnA at 345 MeV u^{-1} [115], a beam intensity of 5×10^5 s^{-1} would be expected for ^{105}Mo. Radioactive ion beams of tungsten were reported from the FRS at GSI, which were produced from ^{238}U- [116] or ^{208}Pb-beam at 1 GeV u^{-1} [117]. Alternative means for the production of a wide range of tungsten isotopes are multinucleon transfer reactions [118] or fusion-evaporation reactions. Based on calculated production cross section, target thickness and primary beam intensity as given in [116], a beam intensity in the order of $\sim 10^4$ s^{-1} would have been expected for the isotope ^{174}W at the FRS.

4 Outlook

Following this study, we have started to experimentally investigate the feasibility of the concept. A target unit was built,

which allows the characterization of the neutron converter setup and the in-target production rates along with beam-induced breakup of carbonyl compounds.

The recently started development of a two chamber approach for the synthesis of carbonyl compounds is not yet included in the considerations of this work [119]. Within this approach, the target foils can be directly irradiated by the proton beam. The nuclear reaction products are flushed with an inert gas stream into a second chamber, in which the radioactive atoms are allowed to react with carbon monoxide to form carbonyl compounds. In this setup a transport efficiency between the two chambers of more than 50% was measured. The spatial separation of isotope production and molecule formation would allow benefiting from higher in-target production rates and avoids exposure of delicate compounds to strong radiation fields at the same time.

---

[8] The actual intensity of the post-accelerated beam depends on additional factors such as presence of isobaric contaminants, molecular break-up and charge state distribution in the electron beam-ion source (charge breeder).

References

1. O. Kofoed-Hansen, K. Nielsen, Dan. Mat.Fys.Medd **26**, no. 7 (1951)
2. J. Koch, O. Kofoed-Hansen, P. Kristensen, W. Drost-Hansen, Phys. Rev. **76**, 279 (1949)
3. J. Ramos, Nucl. Inst. Methods Phys. Res. Sect. B **463**, 201 (2020)
4. J. Lettry, R. Catherall, G. Cyvoct, P. Drumm, A. Evensen, M. Lindroos, O. Jonsson, E. Kugler, J. Obert, J. Putaux et al., Nucl. Inst. Methods Phys. Res. Sect. B **126**, 170 (1997)
5. R. Catherall, W. Andreazza, M. Breitenfeldt, A. Dorsival, G.J. Focker, T.P. Gharsa, G.T. J, J.L. Grenard, F. Locci, P. Martins et al., Journal of Physics G: Nuclear and Particle Physics **44**, 094002 (2017)
6. L. Zanini, M. Andersson, P. Everaerts, M. Fallot, H. Frånberg, F. Gröschel, C. Jost, T. Kirchner, Y. Kojima, U. Köster et al., AIP Conf. Proc. **769**, 1525 (2005)
7. C. Elschenbroich, *Organometallchemie*, Teubner Studienbücher Chemie (Vieweg+Teubner Verlag, 2009), ISBN 9783835192232
8. *The ISOLDE yield database*, http://isolde.web.cern.ch (2018), [Online; accessed 24-August-2018]
9. C.F. Liang, P. Paris, D. Bucurescu, S. Della Negra, J. Obert, J.C. Putaux, Zeitschrift für Physik A Atoms and Nuclei **309**, 185 (1982)
10. Y.I. Frenkel, *Statisticheskaya Fizika (Statistical physics)* (Izd Akad Nauk SSSR, Moskva, 1948)
11. J. Frenkel, Zeitschrift für Physik **26**, 117 (1924)
12. M. Schädel, D. Shaughnessy, eds., *The Chemistry of Superheavy Elements* (Springer Berlin Heidelberg, 2014), https://doi.org/10.1007/978-3-642-37466-1
13. U. Köster, P. Carbonez, A. Dorsival, J. Dvorak, R. Eichler, S. Fernandes, H. Frånberg, J. Neuhausen, Z. Novackova, R. Wilfinger et al., Euro Phys J Spec Topics **150**, 285 (2007)
14. U. Köster, O. Arndt, E. Bouquerel, V. Fedoseyev, H. Frånberg, A. Joinet, C. Jost, I. Kerkines, R. Kirchner, Nucl. Inst. Methods Phys. Res. Sect. B **266**, 4229 (2008)
15. J. Ballof, C. Seiffert, B. Crepieux, Ch.E. Düllmann, M. Delonca, M. Gai, A. Gottberg, T. Kröll, R. Lica, M.M. Flores et al., Euro. Phys. J A **55**, 65 (2019)
16. C.F. Liang, P. Paris, M.G. Porquet, J. Obert, J.C. Putaux, Zeitschrift für Physik A Atoms and Nuclei **321**, 695 (1985)
17. P. Kunz, *The ISAC yield database*, http://mis.triumf.ca/science/planning/yield/beam (2020), [Online; accessed 22-April-2020]
18. F. Baumgärtner, P. Reichold, Z. Naturforsch. **16a**, 945 (1961)
19. G.K. Wolf, W. Fröschen, Tech. Rep. KFK 1783, Kernforschungszentrum Karlsruhe, Zyklotron-Laboratorium, Karlsruhe (1973)
20. K. Bächmann, *Chemical Problems of the On-Line Separation of Short-Lived Nuclides*, in *Proceedings of the 7th international conference on electromagnetic isotope separators and the technique of their applications* (1970), p. 126
21. J. Even, A. Yakushev, Ch.E. Düllmann, J. Dvorak, R. Eichler, O. Gothe, W. Hartmann, D. Hild, E. Jäger, J. Khuyagbaatar et al., Radiochimica Acta **102**, 1093 (2014)
22. J. Even, A. Yakushev, Ch.E. Düllmann, J. Dvorak, R. Eichler, O. Gothe, D. Hild, E. Jäger, J. Khuyagbaatar, J.V. Kratz et al., Inorganic Chem. **51**, 6431 (2012)
23. K. Katagiri, A. Noda, K. Suzuki, K. Nagatsu, A.Y. Boytsov, D.E. Donets, E.D. Donets, E.E. Donets, A.Y. Ramzdorf, M. Nakao et al., Rev. Sci. Inst. **86**, 123303 (2015)
24. I. Usoltsev, R. Eichler, Y. Wang, J. Even, A. Yakushev, H. Haba, M. Asai, H. Brand, A.D. Nitto, Ch.E. Düllmann et al., Radiochimica Acta **104**, 141 (2016)
25. I. Usoltsev, R. Eichler, A. Türler, Radiochimica Acta **104**, 531 (2016)
26. Ch.E. Düllmann, K.E. Gregorich, G.K. Pang, I. Dragojevic, R. Eichler, C.M. Folden III, M.A. Garcia, J.M. Gates, D. Hoffman, S.L. Nelson et al., Radiochimica Acta **97**, 403 (2009)
27. Y. Wang, Z. Qin, F.L. Fan, S.W. Fan, F.-Y.and Cao, X.L. Wu, X. Zhang, J. Bai, X.J. Yin, L.L. Tian, L. Zhao et al., Radiochimica Acta **102** (2014)
28. Y. Wittwer, R. Eichler, D. Herrmann, A. Türler, Radiochimica Acta **109**, 243 (2021)
29. E. Bouquerel, R. Catherall, M. Eller, J. Lettry, S. Marzari, T. Stora, I. Collaboration, Euro. Phys. J. Spec. Topics **150**, 277 (2007)
30. J. Even, A. Yakushev, Ch.E. Düllmann, H. Haba, M. Asai, T.K. Sato, H. Brand, A.D. Nitto, R. Eichler, F.L. Fan et al., Science **345**, 1491 (2014)
31. Ch.E. Düllmann, K.E. Gregorich, G.K. Pang, I. Dragojevic, R. Eichler, C. Folden III., M.A. Garcia, J.M. Gates, D. Hoffman, S.L. Nelson et al., Radiochimica Acta **97**, 403 (2009)
32. M. Götz, A. Yakushev, S. Götz, A.D. Nitto, Christoph E. Düllmann, M. Asai, B. Kindler, J. Krier, B. Lommel, Y. Nagame et al., Radiochimica Acta (2021), https://doi.org/10.1515/ract-2021-1028, available ahead of print
33. R. Catherall, J. Lettry, S. Gilardoni, U. Köster, Nucl. Inst. Methods Phys. Res. Sect. B **204**, 235 (2003)
34. T. Stora, E. Noah, R. Hodak, T.Y. Hirsh, M. Hass, V. Kumar, K. Singh, S. Vaintraub, P. Delahaye, H. Frånberg-Delahaye et al., EPL (Europhysics Letters) **98**, 32001 (2012)
35. J. Ramos, M. Ballan, L. Egoriti, D. Houngbo, S. Rothe, R. Augusto, A. Gottberg, M. Dierckx, L. Popescu, S. Marzari et al., Nucl. Inst. Methods Phys. Res. Sect. B **463**, 357 (2020)
36. R. dos Santos Augusto, L. Buehler, Z. Lawson, S. Marzari, M. Stachura, T. Stora, CERN-MEDICIS collaboration, Appl. Sci. **4** 265 (2014)
37. R. Luis, J.G. Marques, T. Stora, P. Vaz, L. Zanini, Euro. Phys. J. A **48** (2012)
38. A. Gottberg, T. Mendonca, R. Luis, J. Ramos, C. Seiffert, S. Cimmino, S. Marzari, B. Crepieux, V. Manea, R. Wolf et al., Nucl. Inst. Methods Phys. Res. Sect. B **336**, 143 (2014)
39. J. Bennett, C. Densham, P. Drumm, W. Evans, M. Holding, G. Murdoch, V. Panteleev, Nucl. Inst. Methods Phys. Res. Sect. B **126**, 117 (1997)
40. D. Stoychev, A. Papoutsis, A. Kelaidopoulou, G. Kokkinidis, A. Milchev, Materials Chem. Phys. **72**, 360 (2001)

41. T.T. Böhlen, F. Cerutti, M.P.W. Chin, A. Fassò, A. Ferrari, P.G. Ortega, A. Mairani, P.R. Sala, G. Smirnov, V. Vlachoudis, Nucl. Data Sheets **120**, 211 (2014)

42. A. Ferrari, P.R. Sala, A. Fassò, J. Ranft, *FLUKA: A multi-particle transport code*, CERN Yellow Reports: Monographs (CERN, Geneva, 2005), http://cds.cern.ch/record/898301

43. S. Lukić, F. Gevaert, A. Kelić, M. Ricciardi, K.H. Schmidt, O. Yordanov, Nuclear instruments and methods in physics research aection A: accelerators. Spectrometers Detectors Associated Equipment **565**, 784 (2006)

44. A. Koning, D. Rochman, Nuclear Data Sheets **113**, 2841 (2012), special Issue on Nuclear Reaction Data

45. A. Koning, S. Hilaire, S. Goriely, *Talys-1.95, a nuclear reaction program*, https://www.talys.eu

46. K.H. Schmidt, B. Jurado, C. Amouroux, Tech. rep., Organisation for Economic Co-Operation and Development (2014)

47. K.H. Schmidt, B. Jurado, *GEF – A General Description of Fission Observables*, http://www.khs-erzhausen.de/GEF.html, version 2019/1.1, [Online; accessed 21-February-2019]

48. A. Kelic, M.V. Ricciardi, K.H. Schmidt, *ABLA07 - towards a complete description of the decay channels of a nuclear system from spontaneous fission to multifragmentation*, in *Joint ICTP-IAEA Advanced Workshop on Model Codes for Spallation Reactions Trieste, Italy, February 4-8, 2008* (2009), 0906.4193

49. T.E. Cocolios, B.A. Marsh, V.N. Fedosseev, S. Franchoo, G. Huber, M. Huyse, A.M. Ionan, K. Johnston, U. Köster, Y. Kudryavtsev et al., Nucl. Inst. Methods Phys. Res. Sect. B **266**, 4403 (2008)

50. D. Filges, F. Goldenbaum, *Handbook of Spallation Research* (Wiley VCH Verlag GmbH, 2009), ISBN 3527407146

51. J.F. Ziegler, M. Ziegler, J. Biersack, Nuclear Instruments and Methods in Physics Research Section B: Beam Interactions with Materials and Atoms **268**, 1818 (2010), 19th International Conference on Ion Beam Analysis

52. J.F. Ziegler, *SRIM - The Stopping Range of Ions in Matter* , http://www.srim.org (2018), [Online; accessed 24-August-2018]

53. B. Eichler, V.P. Domanov, J. Radioanal. Chem. **28**, 143 (1975)

54. W.M. Haynes, *Handbook of chemistry and physics*, 91st edn. (CRC Press, New York, NY, 2010)

55. J. Powell, F.Q. Guo, P.E. Haustein, R. Joosten, R.M. Larimer, C. Lyneis, D.M. Moltz, E.B. Norman, J.P. O'Neil, M.W. Rowe et al., *BEARS: radioactive ion beams at LBNL*, in *Exotic nuclei and atomic masses (ENAM 98)* (ASCE, 1998)

56. J. Pitters, M. Breitenfeldt, H. Pahl, A. Pikin, F. Wenander, Nucl. Inst. Methods Phys. Res. Sect. B **463**, 198 (2020)

57. A.Y. Boytsov, D.E. Donets, E.D. Donets, E.E. Donets, K. Katagiri, K. Noda, D.O. Ponkin, A.Y. Ramzdorf, V.V. Salnikov, V.B. Shutov, Rev. Sci. Inst. **86**, 083308 (2015)

58. J. Pitters, M. Breitenfeldt, F.J.C. Wenander, H. Pahl, A. Pikin, Tech. rep. (2018), http://cds.cern.ch/record/2648691

59. J. Even, Ph.D. thesis, Johannes Gutenberg-Universität Mainz (2011)

60. S. Cao, Y. Wang, Z. Qin, F. Fan, H. Haba, Y. Komori, X. Wu, C. Tan, X. Zhang, Phys. Chem. Chem. Phys. **18**, 119 (2016)

61. Y. Wang, Z. Qin, F.L. Fan, H. Haba, Y. Komori, S.W. Cao, X.L. Wu, C.M. Tan, Phys. Chem. Chem. Phys. **17**, 13228 (2015)

62. Y. Wang, S. Cao, J. Zhang, F. Fan, J. Yang, H. Haba, Y. Komori, T. Yokokita, K. Morimoto, D. Kaji et al., Phys. Chem. Chem. Phys. **21**, 7147 (2019)

63. I. Zvara, Radiochim. Acta **38**, 95 (1985)

64. J.C. Giddings, *Dynamics of chromatography* (Marcel Dekker Inc, New York, 1965)

65. I. Zvára, *The Inorganic Radiochemistry of Heavy Elements* (Springer Netherlands, 2008), https://doi.org/10.1007/978-1-4020-6602-3

66. J. Ballof, Ph.D. thesis, Johannes Gutenberg - Universität Mainz (2021), http://doi.org/10.25358/openscience-6636

67. T. Stora, *Radioactive Ion Sources*, in *CAS-CERN Accelerator School: Ion Sources, Senec, Slovakia, 29 May - 8 June 2012, edited by R. Bailey* (2014), p. 19, http://cds.cern.ch/record/1693046

68. B. Marsh, *Resonance Ionization Laser Ion Sources*, in *CAS-CERN Accelerator School: Ion Sources, Senec, Slovakia, 29 May - 8 June 2012, edited by R. Bailey* (2014), p. 61, http://cds.cern.ch/record/1693046

69. Y.J. Chen, C.L. Liao, C.Y. Ng, J. Chem. Phys. **107**, 4527 (1997)

70. S. Masuda, Y. Harada, J. Chem. Phys. **96**, 2469 (1992)

71. B.E. Bursten, D.J. Darensbourg, G.E. Kellogg, D.L. Lichtenberger, Inorganic Chem. **23**, 4361 (1984)

72. G.D. Michels, G.D. Flesch, H.J. Svec, Inorganic Chem. **19**, 479 (1980)

73. K.E. Lewis, D.M. Golden, G.P. Smith, J. Am. Chem. Soc. **106**, 3905 (1984)

74. A.W. Ehlers, G. Frenking, J. Am. Chem. Soc. **116**, 1514 (1994)

75. M. Iliaš, V. Pershina, Inorganic Chem. **56**, 1638 (2017)

76. R. Kirchner, E. Roeckl, Nucl. Inst. Methods **133**, 187 (1976)

77. L. Penescu, R. Catherall, J. Lettry, T. Stora, Revi. Sci. Inst. **81**, 02A906 (2010)

78. L.C. Penescu, *Techniques to produce and accelerate radioactive ion beams. tehnici de producere si accelerare a fasciculelor radioactive* (2009), http://cds.cern.ch/record/2259078

79. D.H. Kwon, Y.J. Rhee, Y.K. Kim, Int. J. Mass Spectrometry **245**, 26 (2005)

80. J.C. Jaeger, **11**, 132 (1953)

81. C.M. Verber, A.H. Adelman, J. Appl. Phys. **36**, 1522 (1965)

82. P. Musumeci, L. Cultrera, M. Ferrario, D. Filippetto, G. Gatti, M.S. Gutierrez, J.T. Moody, N. Moore, J.B. Rosenzweig, C.M. Scoby et al., Phys. Rev. Lett. **104**, 084801 (2010)

83. S. Mittelmann, J. Oelmann, S. Brezinsek, D. Wu, H. Ding, G. Pretzler, Appl. Phys. A **126** (2020)

84. P.W.E. Acree, *NIST Chemistry WebBook, NIST Standard Reference Database 69* (National Institute of Standards and Technology, 1997), chap. Mass Spectra

85. T. Srinivasan-Rao, J. Fischer, T. Tsang, J. Appl. Phys. **69**, 3291 (1991)

86. J. Ballof, M. Au, E. Barbero, K. Chrysalidis, C.E. Düllmann, V. Fedosseev, E. Granados, R. Heinke, B. Marsh, M. Owen et al. (2021), accepted for publication in the Proceedings of the International Conference for Ion Sources 2021, 2110.00651

87. C.D. Child, Phys. Rev. (Series I) **32**, 492 (1911)

88. I. Langmuir, Phys. Rev. **2**, 450 (1913)

89. Á. Valfells, D.W. Feldman, M. Virgo, P.G. O'Shea, Y.Y. Lau, Phys. Plasmas **9**, 2377 (2002)

90. Y.Y. Lau, Physical Review Letters **87** (2001)

91. S. Kong, J. Kinross-Wright, D. Nguyen, R. Sheffield, Nuclear instruments and methods in physics research section A: accelerators. Spectrometers Detectors Associated Equipment **358**, 272 (1995)

92. R. Heinke, T. Kron, S. Raeder, T. Reich, P. Schönberg, M. Trümper, C. Weichhold, K. Wendt, Hyperfine Interactions **238** (2016)

93. C.S.R. Nathala, A. Ajami, W. Husinsky, B. Farooq, S.I. Kudryashov, A. Daskalova, I. Bliznakova, A. Assion, Appl. Phys. A **122** (2016)

94. L.M. Zheng, Y.C. Du, C.X. Tang, W. Gai, Chinese Phys. C **41**, 067002 (2017)

95. H. Xuan, H. Igarashi, S. Ito, C. Qu, Z. Zhao, Y. Kobayashi, Appl. Sci. **8**, 233 (2018)

96. R. Zhao, X. Fu, L. Zhang, S. Fang, J. Sun, Y. Feng, Z. Xu, Y. Wang, Appl. Opt. **56**, 8973 (2017)

97. Z. Burkley, A.D. Brandt, C. Rasor, S.F. Cooper, D.C. Yost, Appl. Opt. **58**, 1657 (2019)

98. Z.N. Burkley, Ph.D. thesis, Colorado State University (2019), https://hdl.handle.net/10217/195311

99. Y. Martinez Palenzuela, *Characterization and optimization of a versatile laser and electron-impact ion source for radioactive ion beam production at ISOLDE and MEDICIS.* (2019), Doctoral Thesis, https://cds.cern.ch/record/2672954

100. F.M. Millan, T. Day Goodacre, A. Gottberg, Nuclear Instruments and Methods in Physics Research Section B: Beam Interactions with Materials and Atoms **463**, 302 (2020)

101. Y. Martinez Palenzuela, B. Marsh, J. Ballof, R. Catherall, K. Chrysalidis, T. Cocolios, B. Crepieux, T. Day Goodacre, V. Fedosseev, M. Huyse et al., Nuclear Instruments and Methods in Physics Research Section B: Beam Interactions with Materials and Atoms **431**, 59 (2018)

102. M.J. Higgins, J.G. Hughes, H.B. Gilbody, F.J. Smith, M.A. Lennon, K.L. Bell, A.E. Kingston, *Atomic and molecular data for fusion ; 3, recommended cross sections and rates for electron impact ionization of atoms and ions: copper to uranium* (Culham Lab., Abingdon, 1989), https://cds.cern.ch/record/203081

103. Y. Itikawa, J. Phys. Chem. Reference Data **44**, 013105 (2015)

104. E. Bouquerel, *Atomic beam merging and suppression of alkali contaminants in multi body high power targets: Design and test of target and ion source prototypes at ISOLDE* (2009), http://cds.cern.ch/record/1259908, Doctoral Thesis

105. S. Chu, L.P. Ekström, R.B. Firestone, *The Lund/LBNL nuclear data search*, [Online; accessed 30-April-2020], http://nucleardata.nuclear.lu.se/toi/

106. K. Chrysalidis, Ph.D. thesis (2019), http://cds.cern.ch/record/2703661

107. D.G. Leopold, V. Vaida, Laser Chem. **3**, 49 (1983)

108. R.C. Dunbar, in *Gas Phase Inorganic Chemistry*, edited by D.H. Russell (Springer Nature, 1989), pp. 323–352, ISBN 0306429721

109. L. Windhorn, T. Witte, J.S. Yeston, D. Proch, M. Motzkus, K.L. Kompa, W. Fuß, Chem. Phys. Lett. **357**, 85 (2002)

110. C. Seiffert, J. Ballof, *Extraction of refractory elements by laser induced breakup and ionisation of molybdenum carbonyls* (2017), Letter of Intent to the INTC, INTC-I-178, https://cds.cern.ch/record/2241995

111. A. di Pietro, K. Riisager, P. van Duppen, J.Phys. G **44**, 044013 (2017)

112. Y. Blumenfeld, T. Nilsson, P.V. Duppen, Physica Scripta **T152**, 014023 (2013)

113. H. Suzuki, T. Kubo, N. Fukuda, N. Inabe, D. Kameda, H. Takeda, K. Yoshida, K. Kusaka, Y. Yanagisawa, M. Ohtake et al., Nucl. Inst. Methods Phys. Res. Sect. B **317**, 756 (2013)

114. Y. Shimizu, N. Fukuda, H. Takeda, H. Suzuki, D. Ahn, N. Inabe, K. Kusaka, M. Ohtake, Y. Yanagisawa, K. Yoshida et al., Nucl. Inst. Methods Phys. Res. Sect. B **463**, 158 (2020)

115. *Expected primary beam currents at RIBF*, https://www.nishina.riken.jp/ribf/accelerator/tecinfo.html (2022), [Online; accessed 11-January-2022]

116. J. Kurcewicz, F. Farinon, H. Geissel, S. Pietri, C. Nociforo, A. Prochazka, H. Weick, J. Winfield, A. Estradé, P. Allegro et al., Phys. Lett. B **717**, 371 (2012)

117. T. Kurtukian-Nieto, J. Benlliure, K.H. Schmidt, L. Audouin, F. Becker, B. Blank, E. Casarejos, F. Farget, M. Fernández-Ordóñez, J. Giovinazzo et al., Phys. Rev. C **89**, 024616 (2014)

118. H.M. Devaraja, S. Heinz, D. Ackermann, T. Göbel, F.P. Heßberger, S. Hofmann, J. Maurer, G. Münzenberg, A.G. Popeko, A.V. Yeremin, The European Physical Journal A **56** (2020)

119. M. Götz, S. Götz, J.V. Kratz, J. Ballof, Ch.E. Düllmann, K. Eberhardt, C. Mokry, D. Renisch, J. Runke, T.K. Sato et al., Radiochimica Acta **109**, 153 (2021)